IEEE Access
Multidisciplinary | Rapid Review | Open Access Journal

Received 29 July 2024, accepted 18 August 2024, date of publication 22 August 2024, date of current version 2 September 2024.

Digital Object Identifier 10.1109/ACCESS.2024.3447654

RESEARCH ARTICLE

Dynamic Analysis and Simulation of Airborne Flexible Net Deployment and Collision Processes

XIANG CHEN, XING WANG, YOU CHEN, AND SIYI CHENG
Aeronautics Engineering College, Air Force Engineering University, Xi'an 710038, China
Corresponding author: Siyi Cheng (afeu_csy@163.com)

ABSTRACT The safety of aviation platforms has always been a major concern in the design of aviation vehicles. Airborne high-speed maneuvering targets are currently the most significant threat to all types of aviation platforms due to their high flexibility and anti-jamming capability. This paper presents a new technology of airborne flexible net for high-speed maneuvering target capture. The analysis of flexible net dynamics in this paper includes two aspects: net-expansion dynamics and capture collision dynamics. To solve the technical difficulties of the airborne unfolding of the flexible net, two symmetric design schemes, namely, the traction method and the rotation method, are developed. The mechanical analyses of the two net-expansion methods are carried out. Meanwhile, this paper establishes a collision dynamics model based on the continuous contact force method, and carries out several collision capture tests using two flexible nets. The results show that a transient acceleration is applied in all directions of the target during the collision, capable of reaching the magnitude of 10^4. The maximum stress inside the target aerodynamic surface reaches the magnitude of GPa, and the strong impact produced in the capture process will cause damage to the aerodynamic parts. Finally, the flight experiments of damaged targets are carried out based on six-degree-of-freedom-model, and the effect of damaged targets on the safety of aircraft platforms after contact collisions is further analyzed. The results of this paper can provide a theoretical reference for the research and development of airborne flexible nets.

INDEX TERMS Contact and collision, dynamics modeling and simulation, finite element analysis, flexible net, multibody system dynamics.

I. INTRODUCTION

The flexible net is a special mesh textile composed of ropes, which has the characteristics of large deformation and non-linearity [1], [2]. Flexible net is a generalized concept with many advantages such as a wide expansion range, simple system structure, relatively low technical difficulty and easy cost control [3], [4]. There are many theoretical research and application fields about the flexible net, but the vast majority of them are aimed at the target threat with the characteristics of low speed and simple motion. Currently, the main applications of flexible nets are: anti-drone, ship anti-torpedo, helicopter anti-missile, and space debris capture [5], [6]. Compared with the above application scenarios, in the air-to-air scenarios with strong confrontation and high complexity, the application of flexible net is more difficult and more factors need to be considered. Especially when dealing with airborne high-speed maneuvering targets such as missiles, some complex situations such as fast relative motion speeds of both sides, strong maneuverability, short reaction time, and complex forces in the airborne net-bomb system, may be encountered [7], [8]. This brings a significant challenge for the application of flexible nets to airborne platforms.

The use of flexible nets on airborne platforms offers a variety of unique advantages: 1. The flexible net is capable of responding to high-speed maneuvering targets in the air of different types and modes of guidance. 2. It can break through

The associate editor coordinating the review of this manuscript and approving it for publication was Zheng H. Zhu.

© 2024 The Authors. This work is licensed under a Creative Commons Attribution-NonCommercial-NoDerivatives 4.0 License.
For more information, see https://creativecommons.org/licenses/by-nc-nd/4.0/

the anti-jamming capability of high-speed maneuvering targets [9], [10] and the information advantage supported by the system [11], which greatly improves the survival rate of airborne platforms such as aircraft. 3. The technology is also applicable to various types of high-value aviation platforms (e.g., stealth aircraft, bombers, drones, etc.). It is insensitive to the complex electromagnetic environment and airborne confrontation scenarios [12], [13]. The research and exploration of airborne flexible net technology has a strong wide application, and it is a useful attempt of a new type of active defense technology.

The whole airborne flexible net contains not only flexible ropes with stretchable and incompressible properties, but also rigid bodies such as traction blocks and rotating axis. Therefore, the system is mechanically a complex system involving rigid-flexible coupling [14], [15]. The overall study of the flexible net dynamics problem can be carried out using both continuous and discrete approaches [16]. The dynamical equations of the continuous method have a partial differential form, and the deformation and internal force distribution of the rope net system can be obtained by solving the equations. Because of the partial differential equations involved, the continuous method is only suitable for rope net systems with a small number of units and simple structures, such as the study of string vibration theory by Bernoulli and Poisson [17]. However, the model proposed by them cannot be applied to net systems with complex shape and geometric relations.

According to the different modeling methods of the discrete element, the discrete model can be divided into the discrete particle model, discrete rigid body model and absolute particle coordinate method [18], [19], [20]. Based on the discrete rigid body model, Zhao et al. established a flexible net tensioning model and verified the validity of the model by conducting experiments with a police net gun [21]; Benvenuto et al. established a space rope net unfolding model, and verified the model through ground and microgravity environmental tests [22].

The collision between an airborne flexible net and a high-speed maneuvering target is a multi-body dynamical process including flexible and rigid bodies, with highly nonlinear, and highly transient characteristics. For the study of such a complex process, Dong and Hong proposed the impulse-momentum method [23]. The state of motion of the system after the collision is obtained by solving the recovery coefficient equation and the generalized impulse-momentum equation. However, this method cannot calculate the magnitude of the collision force and the action process during the collision. Duan used the contact constraint method, and they regarded contact as a contact constraint. When a contact occurs, the corresponding constraint equations are applied in the contact region. However, the numerical solution and calculation of this method are difficult [24]. Hunt and Crossley [25] proposed the continuous contact force method, which induces the idea of collision force by utilizing local contact deformation. And when the embedding occurrence is detected, the corresponding contact force is applied in the embedding region. This method can accurately study the collision forces during the collision process without solving the contact constraint equations. Considering the demand of collision effect study on the action process and numerical calculation of collision force, this paper studies the mechanical characteristics of the collision process, with reference to the modeling idea proposed by Hunt K H.

This paper presents, for the first time, an airborne flexible net technology for high-speed maneuvering targets in the air, which innovates the mechanism of defense against high-speed maneuvering targets. In this paper, two flexible net schemes are proposed and the interception collision model is established. The effectiveness of the flexible nets in intercepting high-speed maneuvering targets on airborne platforms is verified by finite element simulation tests. And the flight and guidance characteristics of the damaged missile are also studied based on the six-degree-of-freedom simulation model.

II. A TYPICAL CONFRONTATION SCENARIO

The airborne flexible net system is mainly composed of close-range detection system, airborne launch system, interceptor unit and computer. The interceptor unit consists of a net shell body and a flexible net, which is folded in a special way inside the net shell body. And the body of the flexible net is made of high-performance fiber materials.

Figure 1 illustrates a typical high-speed maneuvering target confrontation scenario. When the system measures the distance, angle and other information of the target, the system computer completes the prediction of the interception point and guides the airborne launch system to fire the interceptor unit. After arriving at the predicted position, the interceptor unit unfolds the flexible net to form a face-shaped capture area. The flexible net can destroy the tracking guidance and attack process of the target by means of contact collision, deflecting trajectory, detonating fuze and so on. Meanwhile, the system can also launch multiple flexible nets and form a joint network in the air to improve the survivability of aircraft platforms.

III. THE NET EXPANSION DYNANMICS MODEL

The rope net system is a typical nonlinear, multi-flexible body dynamic system, and it is difficult to establish an accurate dynamic model at present. Therefore, the discrete modeling idea is adopted in this paper, and the traction and rotary open net methods are modeled respectively on the basis of the centralized quality models.

A. TRACTION TYPE FLEXIBLE NET

1) CENTRALIZED QUALITY MODELS

Considering the physical properties that the ropes are very flexible and can be pulled but not compressed, this paper uses the concentrated mass-semi-damped spring model to analyze the properties of the ropes. The deformation of the net body is described by the trajectory of the centralized mass, the variation of the internal forces is described by

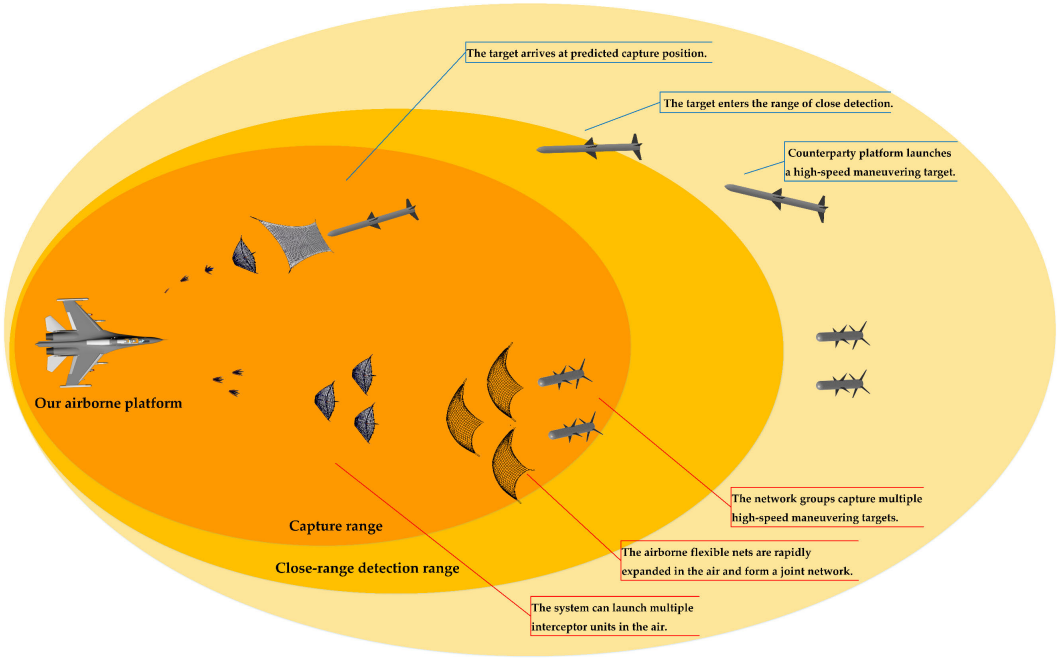

FIGURE 1. A typical confrontation scenario.

the spring-damped unit, and the centralized mass motion is constrained by the spring-damped unit [26].

2) ANALYSIS OF MECHANICAL FORCES

In the force analysis of the rope section, due to the flexible characteristics of the rope section, the internal force equation of the rope section can be expressed as:

$$T_{ij} = \begin{cases} f(l_{ij}, \dot{l}_{ij}) & \dot{l}_{ij} > l_{ij}^0 \\ 0 & l_{ij} \le l_{ij}^0 \end{cases} \tag{1}$$

where l_{ij} represents the actual length of the rope section, and $\dot{l}_{ij}$ represents the rate of change of rope section length.

Further, the rope segment is modeled using a centralized mass-spring model, whose internal force equation can be written as:

$$T_{ij} = \begin{cases} K(l_{ij} - l_{ij}^0) + c\dot{l}_{ij} & l_{ij} > l_{ij}^0 \\ 0 & l_{ij} \le l_{ij}^0 \end{cases} \tag{2}$$

where K and c are the equivalent stiffness and damping coefficient of the centralized mass spring model, respectively. The expression for the equivalent stiffness is:

$$K = \frac{EA_{ij}}{l_{ij}^0} \tag{3}$$

where E is the modulus of elasticity of the flexible net material and A_{ij} is the cross-sectional area of the rope section. The damping coefficient $\boldsymbol{c}$ is expressed as:

$$c = 2\varsigma\sqrt{m_{ij}K} \tag{4}$$

where m_{ij} is the mass of the rope segment and ς is the damping ratio of the rope segment.

The aerodynamic forces subjected to it are investigated in terms of the masses i and j and the rope segment $\mathbf{I}$ between the two masses.

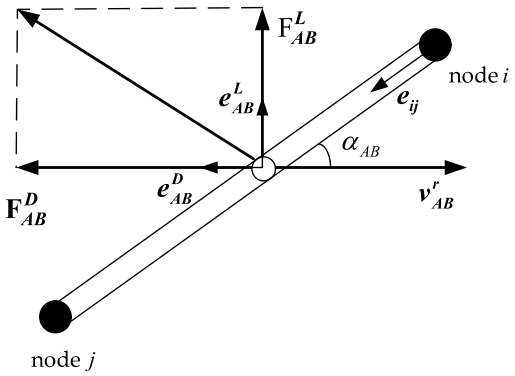

FIGURE 2. The aerodynamic force on the rope segment I.

The aerodynamic force on rope segment $\mathbf{I}$ is decomposed into resistance and lift. The lift force is the component of the aerodynamic combined force in the plumb plane in the direction of the perpendicular airflow.

The expressions for lift $\mathbf{F_{AB}^L}$ and resistance $\mathbf{F_{AB}^D}$ are respectively

$$\mathbf{F_{AB}^D} = \frac{1}{2}\boldsymbol{e}_{\mathbf{AB}}^{\mathbf{D}}\rho_{air}C_{AB}^D d_{ij}\,\|v_{air}\|\,l_{ij} \tag{5}$$

$$\mathbf{F_{AB}^L} = \frac{1}{2}\boldsymbol{e}_{\mathbf{AB}}^{\mathbf{L}}\rho_{air}C_{AB}^L d_{ij}\,\|v_{air}\|\,l_{ij} \tag{6}$$

where ρ_{air} is the density of air, v_{air} is the velocity of the rope segment relative to the air, d_{ij} is the maximum characteristic size of the rope segment, C_{AB}^D and C_{AB}^L are the

coefficients of air resistance and airlift, and $\boldsymbol{e}_{\mathbf{AB}}^{\mathbf{D}}$ and $\boldsymbol{e}_{\mathbf{AB}}^{\mathbf{L}}$ are the unit direction vectors of air resistance and air lift, respectively [27].

$$C_{AB}^{D} = 0.022 + 1.1\sin^3\alpha_{AB} \tag{7}$$

$$C_{AB}^{L} = 1.1\sin^2\alpha_{AB}\cos\alpha_{AB} \tag{8}$$

where α_{AB} is the angle of attack of the rope section.

Thus the resistance and lift forces acting on the mass i are respectively.

$$\mathbf{F}_i^D = \frac{1}{2}\sum_{k\in R(i)}\mathbf{F}_{ik}^D \tag{9}$$

$$\mathbf{F}_i^L = \frac{1}{2}\sum_{k\in R(i)}\mathbf{F}_{ik}^L \tag{10}$$

$R(i)$ contains all the particles that are connected to the particle i.

Based on the previous force analysis, the dynamical equations for any equivalent mass i can be obtained.

$$m_i\ddot{\boldsymbol{r}}_i = \boldsymbol{T}_i + \boldsymbol{F}_i^L + \boldsymbol{F}_i^D + \boldsymbol{G}_i \tag{11}$$

where $\boldsymbol{G}_i$ is the force of gravity acting on the mass i.

B. ROTARY FLEXIBLE NET

The main difference between rotary netting and traction netting is the addition of a center-rotating axis. The rope nets in rotary systems consist of two types: one type connects the mass body and the central rotating axis at each end, called a warp, and the other type spans the adjacent warp and is called a weft. There are two stages involved in the process of rotary net unfolding:

1) STRENGTHENING THE WARP

For theoretical analysis, three coordinate systems are established in Figure 3(a). The origin of the coordinate system $\boldsymbol{e}_x^{(0)} - \boldsymbol{e}_y^{(0)}$ is located in the center of the central axis, and $\boldsymbol{e}_x^{(0)}$ points to the connection between the warp thread and the axis at the initial moment. The origin of the coordinate system $\boldsymbol{e}_x^{(1)} - \boldsymbol{e}_y^{(1)}$ is also located in the center of the central axis and $\boldsymbol{e}_x^{(1)}$ points to the connection between the warp thread and the rotary axis at the current moment. During the unfolding of the net, $\boldsymbol{e}_x^{(1)}$ rotates at an angular velocity of $w = \dot{\theta}$ concerning, and θ is the deflection angle of $\boldsymbol{e}_x^{(1)}$ for $\boldsymbol{e}_x^{(0)}$. The origin of the coordinate system $\boldsymbol{e}_x^{(2)} - \boldsymbol{e}_y^{(2)}$ is at the connection between the tether and the center body, and $\boldsymbol{e}_x^{(2)}$ is along the direction of the warp thread.

In Figure 3(a), φ is the radial declination of the warp thread, i.e., the angle of deflection of $\boldsymbol{e}_x^{(2)}$ to $\boldsymbol{e}_x^{(1)}$. $\boldsymbol{R}$ is the vector pointing from the center of the rotating axis to the mass, $\boldsymbol{r}$ is the vector pointing from the center of the rotating axis to the connection between the warp thread and the rotating axis, along the direction, and $\boldsymbol{L}$ is the vector pointing from the connection to the mass, along the $\boldsymbol{e}_x^{(2)}$ direction.

During the unfolding process, the angular momentum of the central rotating axis $\boldsymbol{\Gamma}$ changes as:

$$\dot{\boldsymbol{\Gamma}} = \boldsymbol{M} + n(\boldsymbol{r}\times\boldsymbol{F}) \tag{12}$$

where $\boldsymbol{M}$ is the control torque applied to the central rotating axis, $\boldsymbol{F}$ is the tension applied to the end of the tether, and n is the number of tethers in the model. Projecting (12) in the rotational direction, it is converted to:

$$J\dot{\boldsymbol{\omega}} = \boldsymbol{M} + n\boldsymbol{F}r_0\sin\varphi \tag{13}$$

where J is the rotational inertia of the center body and r_0 is the radius of the center body. According to Newton's second law, the equations of motion of the mass are:

$$\boldsymbol{F} = m_s\ddot{\boldsymbol{R}} \tag{14}$$

According to the geometrical relations in Figure 3(a) there are:

$$\boldsymbol{R} = \boldsymbol{r} + \boldsymbol{L} \tag{15}$$

Taking the first and second-order derivatives of (15) yields, substituting them into (13) and decomposing Equation into $\boldsymbol{e}_x^{(2)}$ and $\boldsymbol{e}_y^{(2)}$ directions, we can get:

$$\begin{cases} m_s\left[\boldsymbol{r}_0\left(-\omega^2\cos\varphi + \dot{\omega}\sin\varphi\right) + \ddot{\boldsymbol{L}} - \boldsymbol{L}(\omega+\dot{\varphi})^2\right] = -\boldsymbol{F} \\ m_s\left[\boldsymbol{r}_0\left(\omega^2\cos\varphi + \dot{\omega}\sin\varphi\right) + 2(\omega+\dot{\varphi})\dot{\boldsymbol{L}} + \boldsymbol{L}(\dot{\omega}+\ddot{\varphi})\right] = 0 \end{cases} \tag{16}$$

Equation (16) is the rigid body rotation equation and particle motion equation in the case of warp straightening, i.e., hybrid power model.

2) WARP WINDING

The geometry of the warp partially wrapped around the central rotating axis is shown in Figure 3 (b). ϕ represents the angle at which the warp threads are wound on the counter axis and $L - r\phi$ represents the length of the straightened warp threads. The radial deflection angle is satisfied by $\varphi = \pm\frac{\pi}{2}$ when the warp threads are not fully unwound.

At this point, the equation of rotation of the central rotating axis is:

$$J\dot{\boldsymbol{\omega}} = \boldsymbol{M} + n\boldsymbol{F}r_0\sin\varphi \tag{17}$$

In Figure 3(b), the length of the straightened warp thread and the angle of winding ϕ satisfy:

$$L + r\phi = L_{\max} \tag{18}$$

$L_{\max}$ is the maximum length of fully extended. At the origin of the coordinate system $\boldsymbol{e}_x^{(2)} - \boldsymbol{e}_y^{(2)}$, the speed of rotation ω_a is different from the angular speed ω of the central rotating axis due to the change in the length of the meridian. According to the geometrical relations in Figure 3, it is obtained:

$$\begin{cases} \dot{\omega}_a = \dot{\omega} + \ddot{\phi} \\ \dot{\boldsymbol{L}} = -sign(\varphi)\boldsymbol{r}\dot{\phi} \\ \ddot{\boldsymbol{L}} = sign(\varphi)\boldsymbol{r}\ddot{\phi} \end{cases} \tag{19}$$

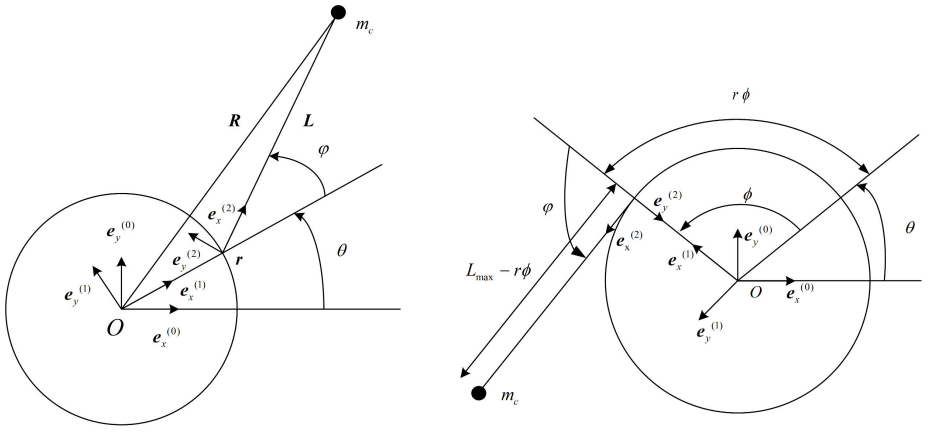

(a) Warp straightening state.

(b) Warp winding state.

FIGURE 3. The geometric relationship between warp threads and the central rotating axis.

The hybrid equation can be obtained by bringing (19) to (16).

IV. CONTACT COLLISION FORCE MODEL

Missile, as a typical high-speed and highly maneuverable airborne target, is the most important threat to aviation platforms. In this section, the intercept collision process is analyzed using a missile target as an example.

The number of equivalent mass points after discretization is denoted by N. $M_i, \boldsymbol{P}_i(t), \boldsymbol{V}_i(t), \boldsymbol{A}_i(t)$, which represents the mass, position, velocity and acceleration vector of the i-th equivalent particle at t time, respectively $i = 1, 2, \cdots, N$.

The position, velocity, and acceleration vectors of the mass point have degrees of freedom in three directions, which can be further decomposed into $p_i(t)$, $v_i(t)$, $a_i(t)$, at this point:

$$\begin{cases} p_{3i+1}(t) = p_{i+1,x}(t) \\ p_{3i+2}(t) = p_{i+1,y}(t) \\ p_{3i+3}(t) = p_{i+1,z}(t) \end{cases} \tag{20}$$

According to the second type of Lagrangian equations, the dynamical equations of the airborne flexible net system can be expressed as:

$$\frac{\mathrm{d}}{\mathrm{d}t}\frac{\partial T}{\partial v_i} - \frac{\partial T}{\partial p_i} + \frac{\partial F}{\partial v_i} + \frac{\partial U}{\partial p_i} = F_i \tag{21}$$

where the force F can be obtained from (16). The kinetic energy, dissipation energy and potential energy of an interceptor system are represented by $T(t), F(t), U(t)$. The kinetic energy $T(t)$ of the flexible net system at moment t is:

$$T(t) = \sum_{i=1}^{N} E_{kini}(t) = \frac{1}{2}\sum_{i=1}^{N} \boldsymbol{V_i}(t)^T M_i \boldsymbol{V_i}(t) \tag{22}$$

Dissipated energy $F(t)$ is:

$$F(t) = \sum_{i=1}^{N} E_{resi}(t) = \frac{1}{2}\sum_{i=1}^{N} \boldsymbol{V_i}(t)^T D \boldsymbol{V_i}(t) \tag{23}$$

where D is the dissipation factor.

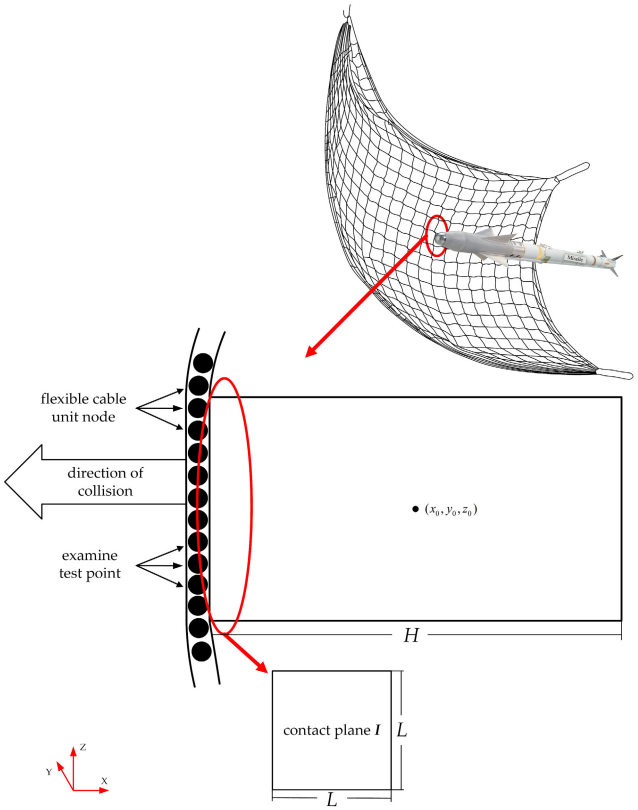

FIGURE 4. The schematic diagram of the collision between the airborne flexible net and the missile.

Gravitational potential energy $U(t)$ is:

$$U(t) = \sum_{i=1}^{N} E_{poti}(t) = \sum_{i=1}^{N} M_i < \boldsymbol{g}, \boldsymbol{P}_i > \tag{24}$$

where $< \boldsymbol{g}, \boldsymbol{P}_i >$ represents the inner product between $\boldsymbol{g}$ and $\boldsymbol{P_i}$.

Before calculating the collision force, it is first necessary to detect whether the airborne flexible net system has collided

with the missile. The basic idea is to determine whether the intrusion has occurred based on the point-plane distance. The points are selected from the net, and since the distribution of equivalent mass points after the discretization of the flexible rope net is relatively sparse, some additional detection points are equally spaced between the equivalent mass points. The surface comes from the missile. Here we take the missile after the cube approximation as an example to establish the mathematical model for detection.

In Figure 4, the length of the cube is H, and the contact plane $\boldsymbol{I}$ is a square with a side length L. Assuming that the coordinates of i-th detection point on the flexible net are (x_i, y_i, z_i), the collision judgment is made based on the distance from the detection point to the centre of the cube. If the distance between the detection point and the center of the cube satisfies:

$$\begin{cases} |x_i - x_0| \le \dfrac{H}{2} \\ |y_i - y_0| \le \dfrac{L}{2} \\ |z_i - z_0| \le \dfrac{L}{2} \end{cases} \tag{25}$$

Then it can be judged that the rope segment where the detection point is located collides with the cube.

When a collision occurs, there is a collision force in the dynamics equation of the flexible net system. In this paper, the continuous contact force method is used to solve the collision force. The continuous contact force method allows intrusions to occur and the magnitude of the collision force is related to the amount of intrusion.

Assuming the i-th detected point collides with the face $\boldsymbol{I}$ of the cube, the analytical expression for this face is: $A_0x + B_0y + C_0z + D_0 = 0$, and the intrusion d_{iI} can be calculated:

$$d_{iI} = \frac{|A_0x_i + B_0y_i + C_0z_i + D_0|}{\sqrt{A_0^2 + B_0^2 + C_0^2}} \tag{26}$$

And the direction of the intrusion $\boldsymbol{n}$ is the direction normal to the $\boldsymbol{I}$-plane, i.e.

$$\boldsymbol{n} = \frac{(A_0, B_0, C_0)}{\sqrt{A_0^2 + B_0^2 + C_0^2}} \tag{27}$$

The collision between the flexible net and the missile will generate two forces, a collision force in the normal direction and a friction force in the tangential direction.

A. COLLISION FORCE

According to the continuous force contact method, the process of collision can be equated by a spring-damper model. When there is a contact collision between the two ends of the spring damper, the spring force is used to simulate the collision force in the contact process, and the damper is used to simulate the energy loss in the collision process.

According to the Hertz collision theory [28], the normal collision force consists of spring restoring force and damping force, and its magnitude is:

$$F^n = \begin{cases} 0 & \delta > 0 \\ K_n\delta^m + C\dot{\delta} & \delta < 0 \end{cases} \tag{28}$$

where K_n is the equivalent contact stiffness, C is the equivalent contact damping coefficient, δ is the normal penetration depth of the contact point. m is the nonlinear contact collision force index (m is usually taken as 1.5).

The equivalent contact damping coefficient C is expressed as:

$$C = \frac{3K_n(1 - e^2)}{4v_k}\delta^m \tag{29}$$

where v_k is the initial collision speed at the moment of contact, e is the coefficient of recovery.

The equivalent contact stiffness is related to the geometry and material properties of the colliding objects at the point of collision and is expressed as:

$$K_n = \frac{4}{3}\left(\frac{1}{R_1} + \frac{1}{R_2}\right)^{-\frac{1}{2}}\left(\frac{1 - \upsilon_1^2}{E_1} + \frac{1 - \upsilon_2^2}{E_2}\right)^{-1} \tag{30}$$

where R_1 and R_2 are the radius of curvature of the contact point on the two contact surfaces respectively, υ_1 is the Poisson's ratio of the net body, υ_2 is the Poisson's ratio of the target body, E_1 is the elastic modulus of the net body, and E_2 is the elastic modulus of the target body. The collision between the flexible net and the missile is a rigid-flexible coupling problem, in which the missile is regarded as a rigid body. Thus the elastic modulus is positive infinity, and the Poisson's ratio is 0. At this time, (29) is transformed into:

$$K_n = \frac{4}{3}\left(\frac{2}{R_2}\right)^{-\frac{1}{2}}\left(\frac{1 - \upsilon_1^2}{E_1}\right)^{-1} \tag{31}$$

B. FRICTION

The magnitude of the friction force is proportional to the extrusion force of the two objects, and in this paper, it is proportional to the collision force. So the friction force F_i^t is:

$$F_i^t = -\mu F_i^n sign\,(\mathrm{v}_i) \tag{32}$$

where μ is the friction coefficient and v_i is the relative tangential velocity between the mass i and the missile contact surface. The friction coefficient μ is related to the roughness of the contact surface and is affected by the relative velocity, which can be measured experimentally.

The solving process of flexible net capturing high-speed maneuvering target can be summarized as Figure 5. According to Section III, the collision-free dynamic simulation is the solution of the dynamic model when the flexible net is unfolded. The solving process includes the analysis of the forces on each mass before the collision occurs, i.e. gravity, aerodynamic forces, tensile forces on other masses, etc. Because the collision force only exists in the collision process between the flexible net and the target, this paper

establishes a collision detection model in section IV. When the flexible net collides with the target, the friction force is solved, and the continuous force contact method is used to analyze the collision force.

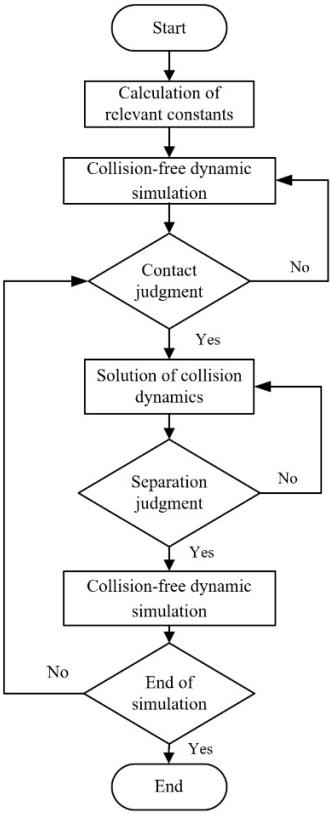

FIGURE 5. The collision dynamics solution process.

V. SIMULATION ANALYSIS

A. PARAMETER SETTING OF FLEXIBLE NET

In this paper, the discretization approach is used to model a nonlinear, multi-flexible and mixed rigid-flexible airborne flexible net system. The LS-DYNA solver is used for the simulation. For the rope segment, the LINK167 unit was chosen. For the mass body and the central rotating axis, the SOLID164 cell is chosen.

For the traction-based net, it uses the classic square mesh and square shape, the net body edge length is 5m; and the mesh edge length is 5cm. And the elastic modulus of the mesh material is 1MPa, the density is 1000kg/m^3. For mass body, the quality of each one is 1kg. And the initial velocity is 100m/s.

This article designs a kind of 8-warp rotary flexible net. In the simulation, the warp length is 3 m, and the mesh radial size is 3cm. For the center rotating axis, the radius is 0.1m, and the quality is 2.8kg. Meanwhile, it was given an initial angular velocity of 10rad/s. For each mass, it has an initial tangential velocity of 30m/s, and the quality is 0.5kg.

In the simulation, it is assumed that the launching height of the interceptor unit is 8 km, and the speed of the interceptor unit is *3Ma* when the flexible net is open. And the atmospheric data such as gravity g and air density ρ are all obtained according to the International Standard Atmospheric Parameter Table.

B. ANALYSIS OF THE UNFOLDING PROCESS

1) TRACTION

The process of traction net unfolding is shown in Figure 6. The figure shows the state of the flexible net system at eight typical moments during the net unfolding process.

It can be seen that the flexible net is pulled by the kinetic energy assembly from a slack state to open. And when the speed of the kinetic energy assembly decreases to 0, the flexible net opens to its maximum. Subsequently, the pulling force on the rope pulls the dynamic component in the opposite direction, and the flexible net contracts. When the net shrinks to a slack state, the dynamic component speed reaches a maximum, and it pulls the flexible net open in the opposite direction according to inertia. This cycle is repeated periodically.

Figure 7 (a) and Figure 7 (b) clearly show the periodic variation of the dynamic component velocity and the rope section tension in the flexible net system, which have the same variation period.

When the speed of the kinetic energy assembly reaches its maximum, the pulling force of the rope segment is 0, and when the pulling force of the rope segment reaches the maximum, the speed of the kinetic energy assembly decreases to 0. This reflects the transition between the internal and kinetic energies of the system during periodic changes in the morphology of the flexible net.

For the airborne flexible net system, the most important indicators are the speed and the area of the flexible net during net expansion. Figure 7(c) reflects that the area of the flexible net also shows an approximate periodic change, and the net can be quickly opened to the maximum within 0.3s, and the maximum area is about 100m^2, which is about four times the initial area.

2) ROTARY UNFOLDING NETS

The process of rotary net unfolding is shown in Figure 8. The figure shows the state of the flexible net system at six typical moments during the net unfolding process.

Similar to the traction flexible net, it can be seen from Figure 9 that the velocity of the kinetic energy assembly and the magnitude of the rope segment tension also show the same periodic variation as the flexible net morphology. The periodicity of the central rotating axis speed is not obvious at the beginning moment. However, with time evolving, the rotation speed of the central rotating axis shows a periodicity consistent with the speed of the kinetic energy assembly and the pulling force of the rope segment. Figure 9(d) reflects that the area of the flexible net also changes approximately

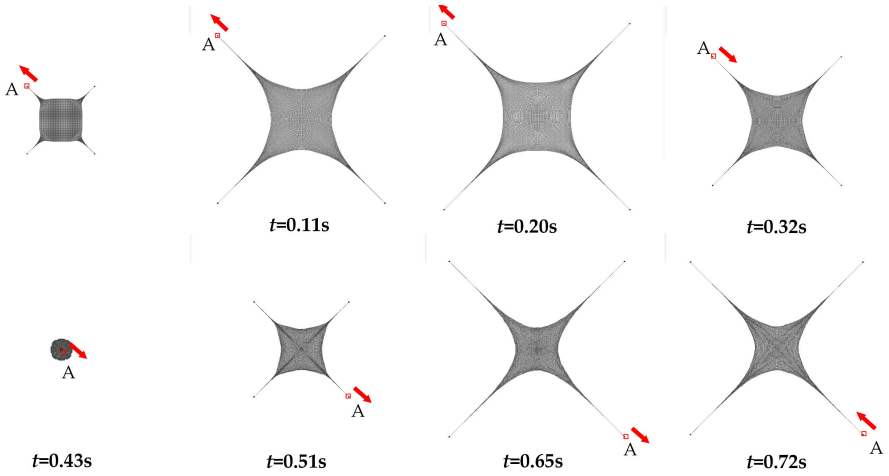

FIGURE 6. The unfolding process diagram of the traction flexible net.

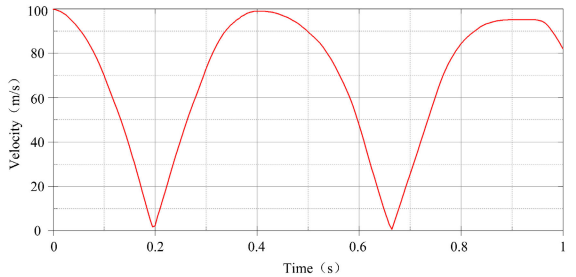

(a) The velocity variation of the kinetic energy assembly.

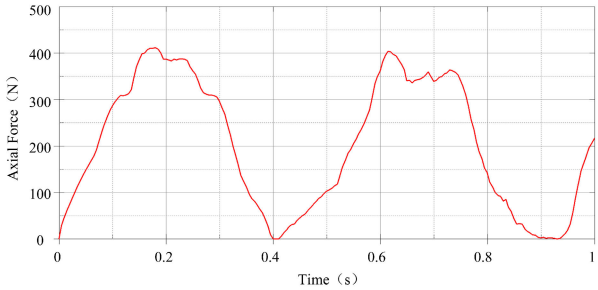

(b) The tension change of the rope segment.

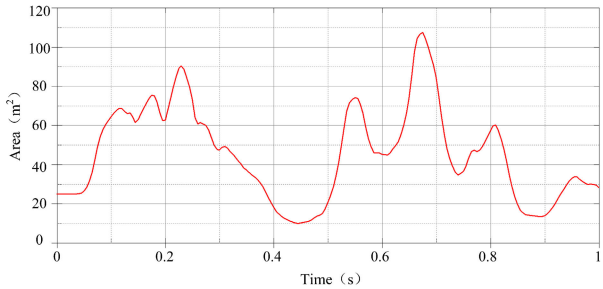

(c) The open area of the flexible net.

FIGURE 7. The change of flexible net components during the opening process.

periodically, and the change period is consistent with the speed of the kinetic energy assembly and the tension of the rope segment. The net can be quickly opened to the maximum within 0.3 seconds, and the maximum area is about 110 m^2, which is about four times the initial area.

To sum up, in these two sets of experiments, both flexible nets can expand to the maximum area in about 0.3 seconds, and the maximum open area is similar. Both nets can be quickly unfolded and formed in the air. This shows that both flexible nets can be suitable for the high-speed maneuvering target confrontation scenario in Figure 1.

C. SIMULATION OF MISSILE CAPTURE PROCESSES OF FLEXIBLE NETS

1) SIMULATION CONFIGURATION

The net shape and material are the same as in Section V-A. As in Section IV, the intercept collision process is also analyzed using missile targets as examples in this section. In order to carry out collision simulation tests, three-dimensional solid models of two kinds of missiles are established: radar type and infrared type, as shown in Figure 10.

The missile model is divided into three parts: the body, the wings and the rudder. Among them, the missile body is modeled by SOLID 164 units, and the wings and the rudder are modeled by SHELL163 units. SHELL163 is a 4-node element with bending characteristics. It can apply plane and normal loads, and output data such as pressure and strain, which can meet the needs of modeling the aerodynamic surface on the missile. The parameters of the missile are shown in Table 1.

Due to the different front-end sensors of the two missiles, the front-end radome shapes of radar missiles and infrared missiles are also different. The two kinds of missiles established in this paper are only different in shape and quality, and other parameters including material and aerodynamic surface parameters are the same.

2) BASIC ASSUMPTIONS FOR SIMULATION

1. Before the collision between the flexible net and the target, the flexible net is in the net-holding stage;

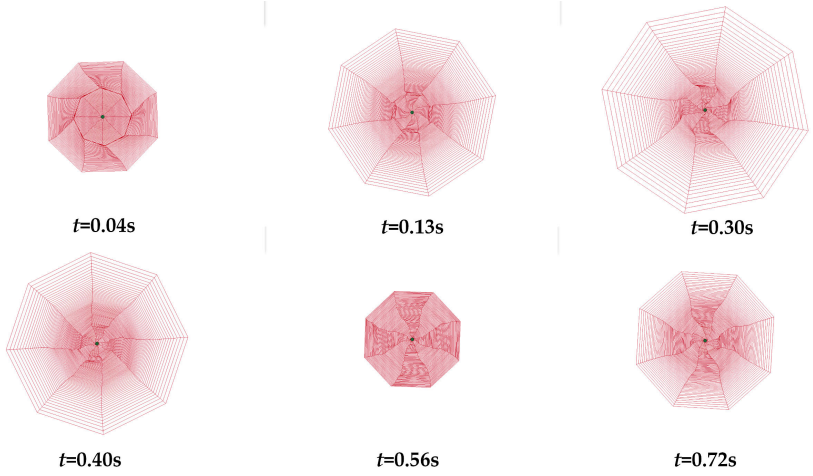

FIGURE 8. The rotary flexible net unfolding process.

TABLE 1. The missile parameters.

Parameters	Numerical value
Length	3.65 m
Diameter	0.178 m
Rudder spread length	0.447 m
Wingspan length	0.445 m
Mass	100 kg

2. The flexible net and the target are in relative linear motion, and the influence of air resistance is not considered in the collision process;
3. For the relative motion between the flexible net and the target, the flexible net is set to static and the target moves toward the flexible net during the simulation.

3) ANALYSIS OF RADAR-TYPE MISSILE INTERCEPTION

In the test, the missile crashed into the flexible net at a speed of 500m/s. In Figure 11, eight typical moments during two collision processes are selected, where the Z-axis points to the direction of the missile's motion, and the Y-axis is along the direction of the lead weight and pointing upwards.

According to the results in Figure 11, after the missile came into contact with the flexible net, the radome as well as the aerodynamic surfaces penetrate directly from the flexible net. After the collision, the net starts to shrink towards the collision point. Since the missile speed is much faster than the size of the missile and the flexible net, the whole collision process time is very short, less than 10ms.

a: TRACTION FLEXIBLE NETS CAPTURE IMPACT ANALYSIS

Firstly, the impact of the collision on the missile is analyzed in terms of kinematics. Figure 12 shows that the total velocity of the missile does not change after the collision, nor does the velocity in the original velocity direction. The collision of the missile produces velocity in the X direction and Y direction, but the velocity in these two directions is less than 1/10000 of the absolute speed, which can be ignored. When the missile is incident perpendicular to the net surface, the collision between the flexible net and the missile mainly generates acceleration in the direction of relative motion. And when the missile is just in contact with the flexible net, the acceleration is maximum, which the value is $195\text{m}/\text{s}^2$.

The attitude change of the missile is characterized by the angle of rotation around three coordinates, in which the rotation angles around the X-axis, Y-axis, and Z-axis reflect the changes in the pitch, yaw, and roll angles of the missile, respectively. From Figure 13, it can be seen that the missile performed a small roll during the collision and stopped after the collision. In addition, the missile's pitch and yaw angles have small changes due to the collision, and the change values are less than 10^{-3} rad.

In addition to the kinematic effects, the impact during the collision process may affect the integrity of the missile. Figure 14 reflects the stress distribution of the missile wing and rudder surfaces at two specific moments, and the results show that the aerodynamic surfaces of the missile generated large internal stresses during the collision process. The maximum stresses inside the aerodynamic surfaces reach the magnitude of GPa. From Figure 14, it is obvious that the aerodynamic surfaces of the missile are deformed by the extrusion of the rope net.

b: ROTARY FLEXIBLE NETS CAPTURE IMPACT ANALYSIS

According to the previous analysis, the collision process has limited influence on the missile's motion state, so the main focus here is on the change in the missile's acceleration during the collision process and the magnitude of the force on the missile's aerodynamic surface.

As can be seen from Figure 15 (a), under the condition that the missile is launched perpendicular to the net, the

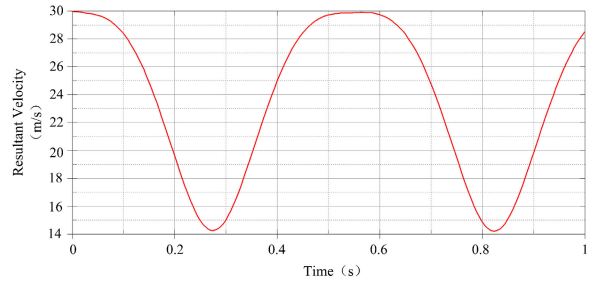

(a) The velocity variation of the kinetic energy assembly.

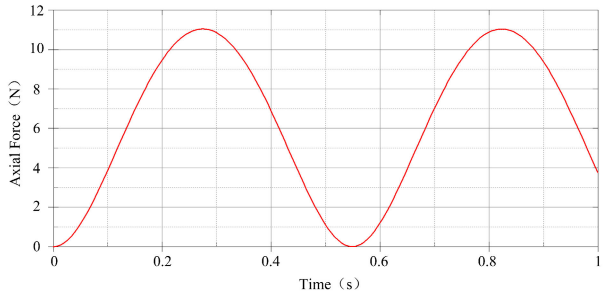

(b) The variation of the rope section tension.

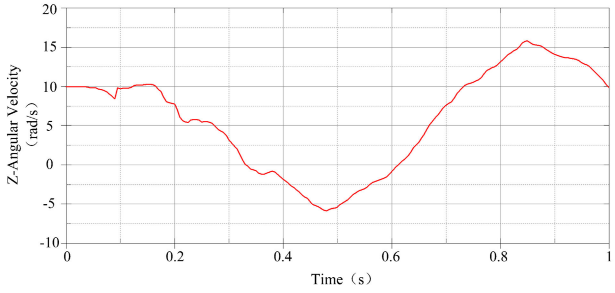

(c) The rotation speed of the central rotating axis.

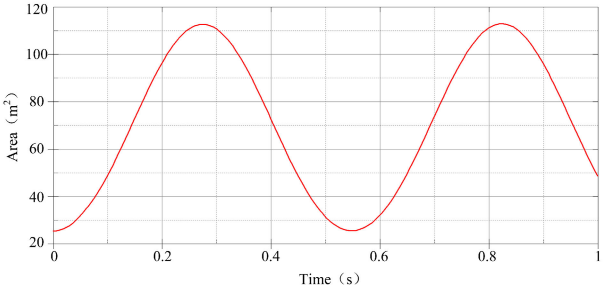

(d) The open area of the flexible net varies with time.

FIGURE 9. The change of flexible net components during the opening process.

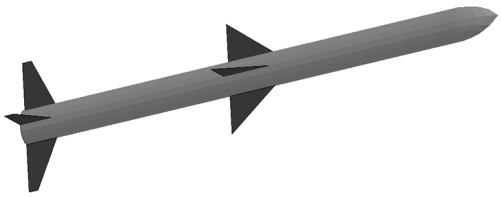

(a) The radar-type missile

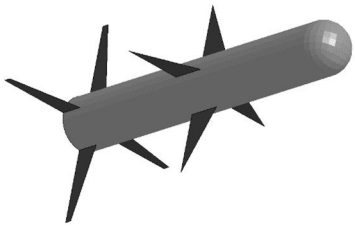

(b) The infrared-type missile

FIGURE 10. Three-dimensional solid models of two missiles.

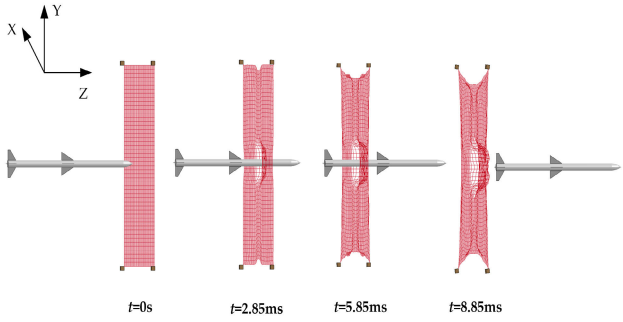

(a) The collision process between the missile and a traction flexible net.

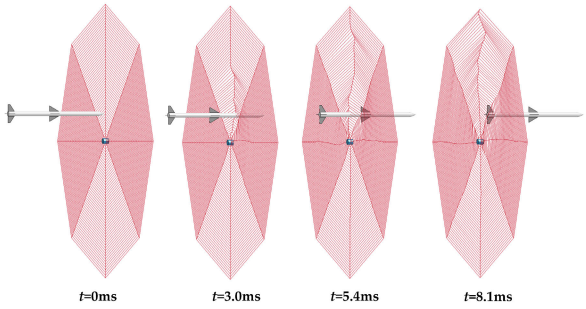

(b) The collision process between the missile and a rotary flexible net.

FIGURE 11. The interception process of radar-type missiles.

acceleration is maximized when the missile makes a first contact with the flexible net. A large acceleration is produced in the relative motion direction, lead hammer direction and horizontal plane, and the maximum value is $80\mathrm{m}/\mathrm{s}^2$. This is due to the special network structure of the rotary flexible network, which makes the acceleration of the missile change greatly in many directions.

Figure 15(b) shows that the maximum stress inside the aerodynamic surface remains in the magnitude of MPa during the whole collision process, with a maximum value of 10.5 MPa, which is much smaller than the permissible stress of the missile body and the aerodynamic surface components, and the damage to the aerodynamic parts is relatively small.

4) ANALYSIS OF THE INFRARED-TYPE MISSILE INTERCEPTION

As can be seen from the analysis in Section V-C, the traction net has a better destructive effect on radar-type missiles. In order to better verify the effect of traction flexible net, this section carries out a collision test between an infrared-type missile and a traction net. The simulation results are shown in Figure 16.

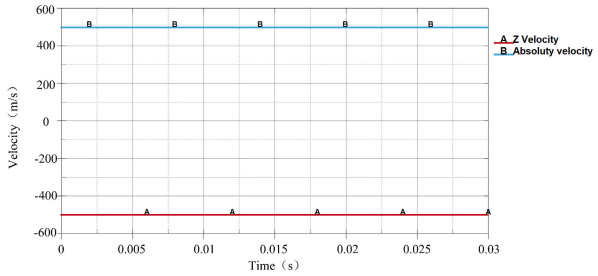

(a) The Missile's absolute velocity and Z-direction velocity.

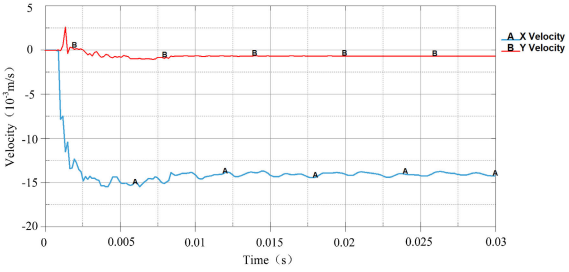

(b) The velocity of the missile in X and Y directions.

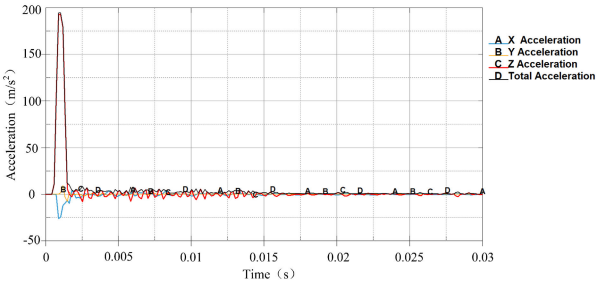

(c) The acceleration variation of the missile in three directions during the collision.

FIGURE 12. The variation of the missile velocity and acceleration.

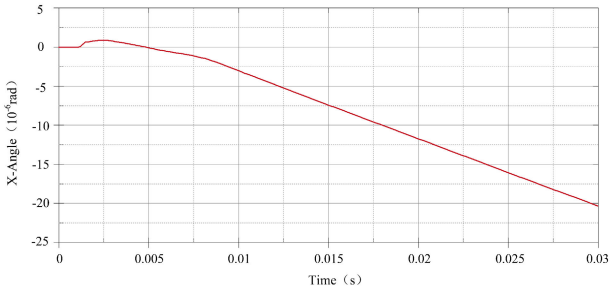

(a) The angle of rotation of the missile around the X-axis.

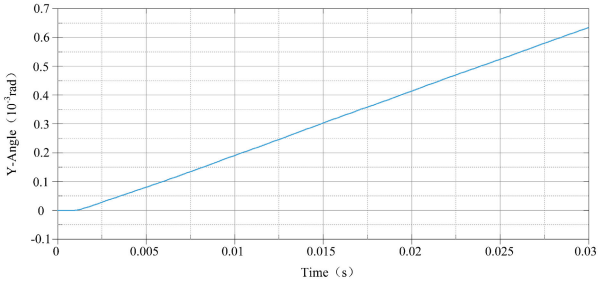

(b) The angle of rotation of the missile around the Y axis.

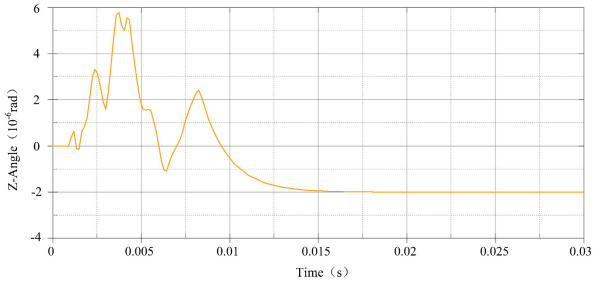

(c) The angle of rotation of the missile around the Z-axis.

FIGURE 13. The attitude change of the missile.

As can be seen from Figure 16, the blunt radome represented by the infrared missile will not pass directly through the flexible net after the collision, and the flexible net is carried forward by the infrared missile in the air. The acceleration of the missile and the maximum stress of the aerodynamic surface are still used as indexes for evaluating the destructive effect, and the simulation results are shown in Figure 17.

As can be seen from Figure 17, the effect of flexible nets on the acceleration of infrared-type missiles is much greater and can reach a magnitude of 10^4. And since the infrared-type missile does not pass through the net during the collision with the flexible net, the stress on the aerodynamic surface is relatively small, but the maximum stress inside the aerodynamic surface during the whole collision process reaches a magnitude of 100 MPa, which is still greater than the permissible stress of general metal.

Summarizing the experiments in Section V-C, the following conclusions can be drawn:

1. The results show that the collision between the flexible net and the missile has a small effect on the missile in terms of kinematics, and the changes in the missile's velocity and attitude can be ignored.

2. Both different flexible nets produced a short-lived acceleration in all directions of the missile, with greater accelerations in the direction of motion for the traction flexible nets.

3. In the process of collision, the maximum stress inside the aerodynamic surface reaches the magnitude of GPa, and the strong impact will destroy the aerodynamic surfaces of the missile. The stress caused by the collision between the missile and the traction flexible net is greater than that caused by the collision with the rotary flexible net. Because the mesh of the traction interception is smaller, the missile needs to undergo more force to pass through the mesh.

VI. THE FLIGHT EXPERIMENT OF THE DAMAGED TARGET BASED ON THE SIX-DEGREE-OF-FREEDOM MODEL

The influence and destructive effect of the contact collision process on a high-speed maneuvering target under the action of the flexible net are analyzed in Section V. The results of the study show that aerodynamic destruction is achievable. Due to the extremely fast movement of the target and the short time of interaction with the flexible net, the change of the motion state and the generation of disturbance can

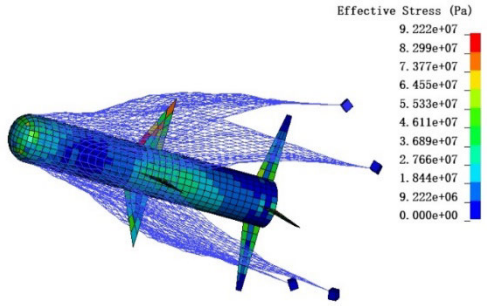

(a) The stress distribution on the missile face and rudder surface at moment 1.

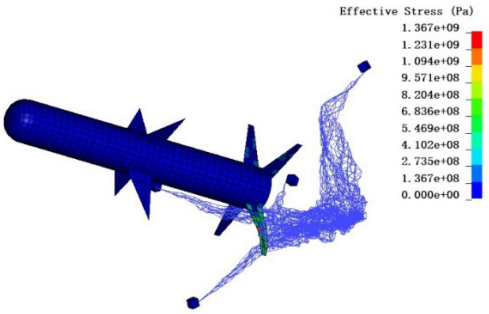

(b) The stress distribution on the missile face and rudder surface at moment 2.

FIGURE 14. The stress distribution on the aerodynamic surface of the missile during the collision process.

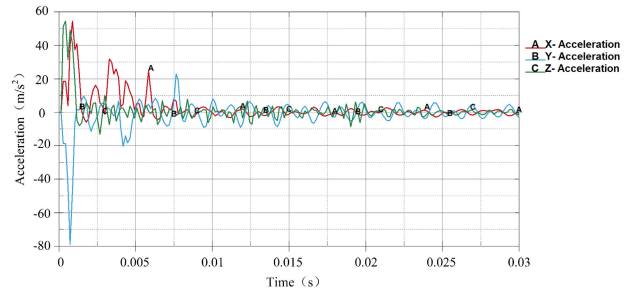

(a) The acceleration of the missile during the collision.

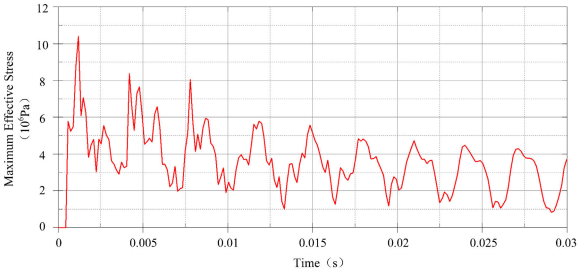

(b) The maximum stress on the aerodynamic surface during collision.

FIGURE 15. The analysis of two effects of rotary flexible nets capture.

be observed, but the two effects are not obvious. Currently, the research based on numerical analysis and wind tunnel tests shows that the damage of aerodynamic surface will lead to the change of aircraft aerodynamic parameters and the decrease of flight performance [29], [30]. In order to further analyse the impact of damaged missiles on the safety of aircraft platforms, this paper refers to the method of Kim and Nguyen [30], [31] and investigates the flight and guidance characteristics of damaged missile targets, using a six-degree-of-freedom simulation model.

The missile target six-degree-of-freedom simulation model includes the target motion module, missile motion module, guide head module, guidance module, control module, and rudder module. The data flow relationship of the whole system is shown in Figure 18.

At the initial moment of the simulation, the initial coordinate of the aircraft platform is [7000m, 0, 0], the initial velocity direction is along the x-axis and the magnitude is 272m/s. After that the aircraft platform will do a hover maneuver and the commanded overload size $n_z = 5$. The initial coordinate of the missile target is located at [4000m,1000m,500m] and the initial velocity is 1000m/s. The missile adopts a proportional guidance method with a guidance constant N=6. Figure 19 shows the trajectories of the missile target and aircraft platform under the condition that the missile is not damaged by the flexible net.

According to the interception collision analysis in Section V, the flexible net mainly causes great damage to the aerodynamic surfaces of the missile wing and rudder surface. First of all, the motion of the target missile is considered when the wing is damaged. When the wing is damaged, for the wing coefficient, the lift coefficient C_y^α and lateral force coefficient C_z^β will decrease, whereas the coefficients of pitch stability moment m_z^α and yaw stability moment m_y^β will increase. It is assumed that the damage to the wing results in a 40% decrease in the lift and lateral force coefficient of the missile, and a 40% increase in the pitch and yaw stability torque coefficient. Simulation experiments are carried out under the same initial conditions, and the results are shown in Figure 20 and Figure 21.

Figure 20 shows that a missile with a damaged wing detaches from its target while attacking an aircraft platform, and Figure 21 reveals the reason for the missile's detachment from its target. Figure 21 (a) (b) shows that after the missile wing is damaged, the actual overload oscillates so violently that it is no longer possible to track the command overload normally. Figure 21 (c) (d) (e) shows that the yaw angle, pitch angle and roll angle of the missile have wobbled violently, the missile has lost its stability, and its attitude has changed dramatically. At this time, the guidance and control system of the missile can no longer work properly.

When the rudder surface of the missile is damaged, the efficiency of the rudder is affected by the decrease of lift and lateral force coefficients, as well as the corresponding decrease of roll, yaw and pitch control moment coefficients. As can be seen from the simulation results in Figure 22, the missile will miss the target only when the rudder surface fails completely and the steering torque coefficient is equal to 0. At this time, the control system of the

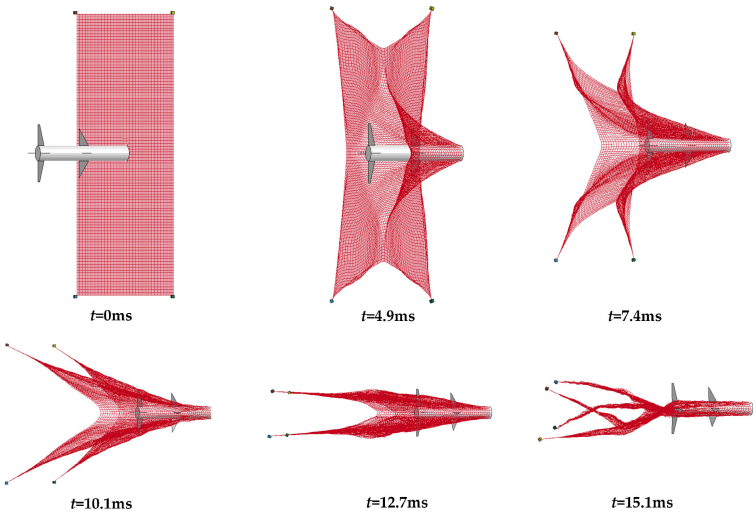

FIGURE 16. The infrared-type missile collision process with the flexible net.

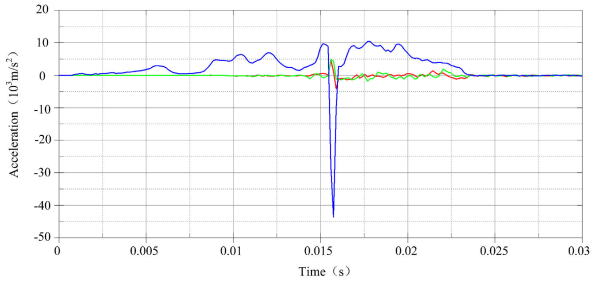

(a) The acceleration of the infrared missile.

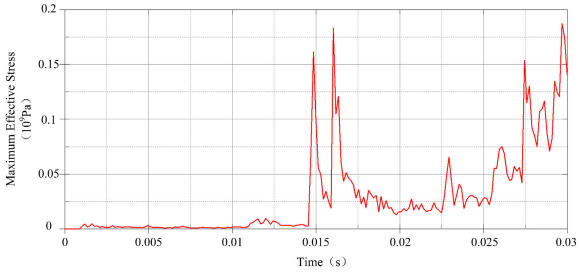

(b) The maximum stress on the aerodynamic surface during collision.

FIGURE 17. The analysis of the infrared-type missile interception.

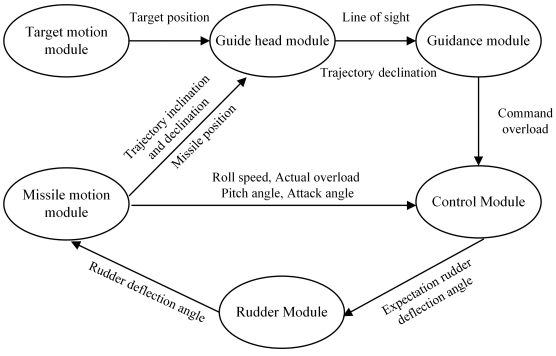

FIGURE 18. The data flow diagram of the missile target six-degree-of-freedom simulation system.

missile fails, and the command overload cannot be tracked effectively.

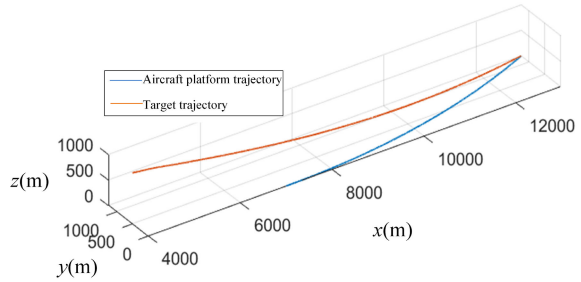

FIGURE 19. The trajectory of the aircraft platform and undamaged target.

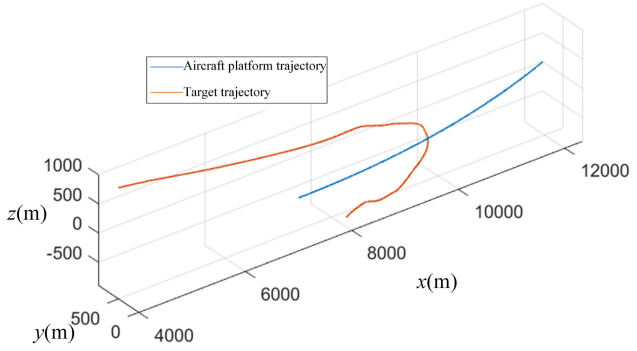

FIGURE 20. The trajectory of the damaged missile.

From the preceding findings, there are many methods to cause the missile to deviate from the target in the process of contact collision. First, the wing surface of the missile is damaged, resulting in the loss of stability and drastic changes in attitude during flight; Second, the missile's rudder is completely damaged and the control system fails to respond to commands. For the first method, damage to the missile wing surface of about 50 per cent will result in off-targeting; for the second method, complete damage to the rudder surface of the missile will result in off-targeting.

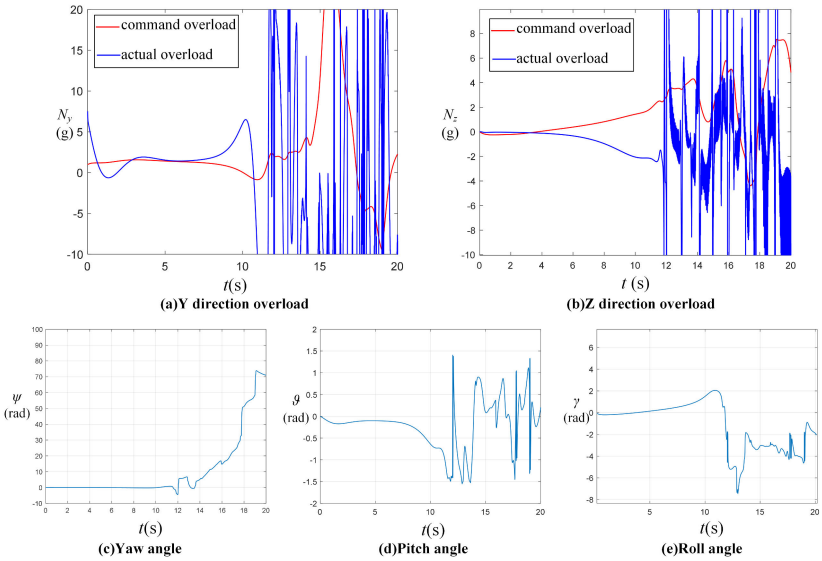

FIGURE 21. The overload and attitude of the damaged missile.

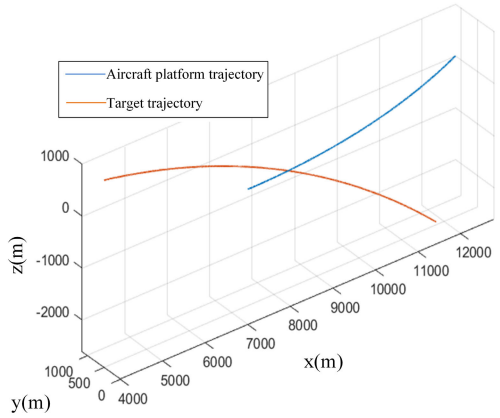

(a) The trajectory of the aircraft platform and the target.

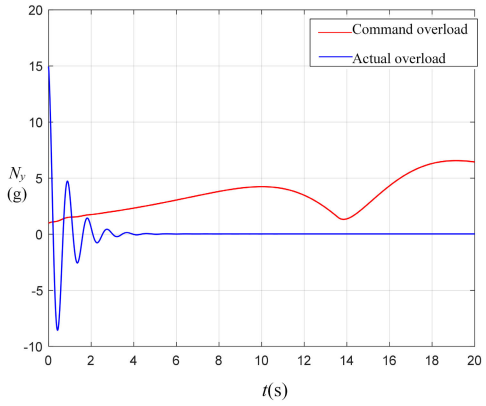

(b) The Y-direction command and the actual overload.

FIGURE 22. The trajectory and overload of the missile in the face of total rudder surface failure.

VII. SUMMARY

A typical application scenario of the flexible nets intercepting high-speed maneuvering targets was first constructed. In order to solve the technical difficulties of the airborne unfolding of the flexible net, two symmetric design schemes were proposed. Simulation results show that the flexible nets of both methods can be expanded quickly, and alternately present the tensioning and contracting states. Based on the flexible nets, this paper proposed an intercepting collision model. From several sets of experiments, it can be summarized that in the process of collision, the flexible net has little influence on the missile in terms of kinematics, but has a greater influence on the acceleration in all directions of the missile and the stress inside the aerodynamic surface. From the six-degree-of-freedom simulation experiments, damage to both the wing and rudder aerodynamic surfaces of the missile disables the missile control system. The missile exhibits an ineffective response to control commands, which consequently results in a failure to maintain trajectory accuracy and thus missing the intended target. The research results of this paper can provide a theoretical reference for the application of airborne flexible net technology in the interception of high-speed maneuvering targets, and provide new ideas for the safety and security of aviation platforms.

INTEREST STATEMENT

The authors declared that there is no competing interest.

DATA AVAILABILITY STATEMENT

Data are made available on reasonable request.

REFERENCES

[1] E. M. Botta, C. Miles, and I. Sharf, "Simulation and tension control of a tether-actuated closing mechanism for net-based capture of space debris," *Acta Astronautica*, vol. 174, pp. 347–358, Sep. 2020.

[2] G. S. Aglietti, B. Taylor, S. Fellowes, T. Salmon, I. Retat, A. Hall, T. Chabot, A. Pisseloup, C. Cox, A. Zarkesh, A. Mafficini, N. Vinkoff, K. Bashford, C. Bernal, F. Chaumette, A. Pollini, and W. H. Steyn, "The active space debris removal mission remove debris. Part 2: In orbit operations," *Acta Astronautica*, vol. 168, pp. 310–322, Jan. 2020.

[3] Y. Liu, Z. Xiong, Y. Qiu, F. Yan, and C. Ma, "Analysis of traction and unfolding dynamics of space-symmetric flexible webs for UAV interception and capture," *Symmetry*, vol. 14, no. 9, p. 1915, Sep. 2022.
[4] B. Xu, Y. Yang, Y. Yan, and B. Zhang, "Bionics design and dynamics analysis of space webs based on spider predation," *Acta Astronautica*, vol. 159, pp. 294–307, Jun. 2019.
[5] E. M. Botta, I. Sharf, A. K. Misra, and M. Teichmann, "On the simulation of tether-nets for space debris capture with vortex dynamics," *Acta Astronautica*, vol. 123, pp. 91–102, Jun. 2016.
[6] M. Ru, Y. Zhan, B. Cheng, and Y. Zhang, "Capture dynamics and control of a flexible net for space debris removal," *Aerospace*, vol. 9, no. 6, p. 299, Jun. 2022.
[7] W. J. O'Connor and D. J. Hayden, "Detumbling of space debris by a net and elastic tether," *J. Guid., Control, Dyn.*, vol. 40, no. 7, pp. 1832–1836, Jul. 2017.
[8] M. Shan, J. Guo, and E. Gill, "Deployment dynamics of tethered-net for space debris removal," *Acta Astronautica*, vol. 132, pp. 293–302, Mar. 2017.
[9] R. R. Kumar, H. Seywald, and E. M. Cliff, "Near-optimal three-dimensional air-to-air missile guidance against maneuvering target," *J. Guid., Control, Dyn.*, vol. 18, no. 3, pp. 457–464, May 1995.
[10] Y. Li, Y. Lyu, J. Shi, and W. Li, "Autonomous maneuver decision of air combat based on simulated operation command and FRV-DDPG algorithm," *Aerospace*, vol. 9, no. 11, p. 658, Oct. 2022.
[11] A. Ratnoo and T. Shima, "Guidance strategies against defended aerial targets," *J. Guid., Control, Dyn.*, vol. 35, no. 4, pp. 1059–1068, Jul. 2012.
[12] G. Frazer, A. Balleri, and G. Jacob, "Deception jamming against Doppler beam sharpening radars," *IEEE Access*, vol. 8, pp. 32792–32801, 2020.
[13] J.-W. Rim and I.-S. Koh, "Survivability simulation of airborne platform with expendable active decoy countering RF missile," *IEEE Trans. Aerosp. Electron. Syst.*, vol. 56, no. 1, pp. 196–207, Feb. 2020.
[14] L. A. Bilich, S. A. Lyovin, and V. V. Ostapova, "Air-to-air missile guidance for nonmaneuverable target interception at maximum distance," *TsAGI Sci. J.*, vol. 49, no. 7, pp. 753–770, 2018.
[15] Y. Liu, Z. Xiong, J. Wang, and D. Wang, "Monte Carlo-based analysis and experimental validation of the interception-damage probability of the new active interception net," *Math. Problems Eng.*, vol. 2022, pp. 1–12, Aug. 2022.
[16] P. Flores, "Contact mechanics for dynamical systems: A comprehensive review," *Multibody Syst. Dyn.*, vol. 54, no. 2, pp. 127–177, Feb. 2022.
[17] Q. Q. Chen, Z. W. Feng, and G. B. Zhang, "Dynamic modeling and simulation of anti-UAV rope web capture system," *J. Natl. Univ. Defense Technol.*, vol. 44, pp. 9–15, 2022.
[18] V. Udoewa and V. Kumar, "Computational fluid dynamics," in *Applied Computational Fluid Dynamics*. Hoboken, NJ, USA: Wiley, 2012.
[19] A. Valkeap, K. M. Matikainen, and M. A. Mikkola, "Meshing strategies in the absolute nodal coordinate formulation-based Euler-Bernoulli beam elements," *PI Mech. Eng. K-J MUL*, vol. 230, no. 4, pp. 606–614, 2016.
[20] A. Shabana, "An Absolute nodal coordinate formulation for the large rotation and deformation analysis of flexible bodies," Univ. Illinois, Chicago, IL, USA, Tech. Rep. MBS96-1-UIC, 1996.
[21] G. W. Zhao and H. B. Xiong, "Numerical simulation and experiment on the expansion process of flexible rope body," *J. Aeronaut.*, vol. 30, no. 8, pp. 1429–1434, 2009.
[22] R. Benvenuto, M. Lavagna, and S. Salvi, "Multibody dynamics driving GNC and system design in tethered nets for active debris removal," *Adv. Space Res.*, vol. 58, no. 1, pp. 45–63, Jul. 2016.
[23] F. X. Dong and J. Z. Hong, "A summary of the research on dynamic collision of multibody systems," *Adv. Mech.*, vol. 39, no. 3, pp. 352–359, 2009.
[24] Y. C. Duan and D. G. Zhang, "Rigid-flexible coupling dynamics of a flexible robot with impact," *Adv. Mater. Res.*, vols. 199–200, pp. 243–250, Feb. 2011.
[25] K. H. Hunt and F. R. E. Crossley, "Coefficient of restitution interpreted as damping in vibroimpact," *J. Appl. Mech.*, vol. 42, no. 2, pp. 440–445, Jun. 1975.
[26] K. Amaroju, K. Vijayan, and M. I. Friswell, "Non-linear modal interactions during rub-impact of a rotating flexible shaft," *J. Vibrat. Control*, vol. 29, nos. 7–8, pp. 1554–1563, Apr. 2023.
[27] S. F. Hoerner, *Fluid-Dynamic Drag*. Germany: S. F. Hoerner, 1965, p. 455.
[28] V. L. Popov, *Contact Mechanics and Friction: Physical Principles and Applications*. Cham, Switzerland: Springer, Jan. 2010.
[29] P. M. Render, M. Samaad-Suhaeb, Z. Yang, and M. Mani, "Aerodynamics of battle-damaged finite-aspect-ratio wings," *J. Aircr.*, vol. 46, no. 3, pp. 997–1004, May 2009.
[30] K.-J. Kim, J. Ahn, S. Kim, J.-S. Choi, J. Suk, H. Lim, and G.-B. Hur, "Analysis of partial wing damage on flying-wing unmanned air vehicle," *Proc. Inst. Mech. Eng., G, J. Aerosp. Eng.*, vol. 228, no. 3, pp. 355–374, Mar. 2014.
[31] N. Nguyen, K. Krishnakumar, J. Kaneshige, and P. Nespeca, "Dynamics and adaptive control for stability recovery of damaged asymmetric aircraft," in *Proc. AIAA Guid., Navigat., Control Conf. Exhibition*, 2013, pp. 21–24.

XIANG CHEN was born in Neijiang, Sichuan, China, in 1996. He received the master's degree in weapons science and technology from Air Force Engineering University, Xi'an, in 2022, where he is currently pursuing the Ph.D. degree. His research interests include electronic countermeasure theory and technology, signal processing, and critical target protection technology.

XING WANG is currently a Professor with Air Force Engineering University. His research interests include information technology and electronic countermeasure technology.

YOU CHEN was born in Yueyang, Hunan, China, in 1983. He received the Ph.D. degree from Air Force Engineering University. He is currently an Associate Professor and a Master's Supervisor with Air Force Engineering University. His research interests include electronic countermeasure theory and technology, radar signal processing, and weapon system design.

SIYI CHENG was born in Nanjing, Jiangsu, China, in 1980. He received the degree from Air Force Engineering University, in March 2007, majoring in weapon system design. He is currently a Professor and a Master's Supervisor with Air Force Engineering University. He has long been committed to the theoretical research of aircraft integrated defense technology, missile countermeasure technology, and radar technology.